Large-Scale Discrete-Element Modeling for Engineering Analysis: Case Study for the Mobility Cone Penetrometer

John F. Peters, M.ASCE[1]; Bohumir Jelinek[2]; Clay Goodman, S.M.ASCE[3]; Farshid Vahedifard, M.ASCE[4]; and George Mason, M.ASCE[5]

Abstract: This study aims to examine the use of the discrete-element method (DEM) for prototype-scale analyses of large discontinuous deformations. As an example, this paper presents the results of large-scale modeling of a mobility cone penetration test using DEM. The analysis demonstrates the potential for very-large-scale fully three-dimensional discrete-element computations for simulation of uniquely difficult geotechnical problems involving discontinuous deformation such as cone penetration, plowing, and slope stability. The particle-scale resolution was achieved using several million particles as a straightforward application of high-performance computing with message-passing interface (HPC-MPI) techniques. The use of the discrete-element method for micromechanical studies versus prototype-scale engineering studies are discussed in detail. The former involves accurately depicting details such as particle size distribution and particle shape; the latter uses the computational particles, similar to finite elements, where characteristics of the particles are simplified to gain computational efficiency. The DEM inherently captures qualitative constitutive soil behavior; calibration procedures are directed at achieving accurate quantitative behavior. A key issue is defining the soil's consolidation state because porosity cannot be specified as a material parameter but depends on particle placement and compaction. In addition to cone simulations in the near-surface environment, deep penetration simulations were used to examine the effect of confining stress on volume change. The cone tended to increase porosity at all stress levels, although the increase was significantly subdued by higher stress levels. The particle stress is presented in various formats to illustrate how cone resistance is developed. **DOI:** 10.1061/(ASCE)GT.1943-5606.0002174.

Author keywords: Discrete-element method; Cone penetration test; Stress analysis; Parallel computing; Off-road mobility.

Introduction

Continuum-based numerical methods developed over the past 50 years have become powerful tools for solving difficult geotechnical engineering problems, yet there is a large class of problems involving large discontinuous deformations that tax the capabilities of continuum-based methods. Example problems include materials handling, excavation and plowing, penetration, and landslide prediction.

[1]Associate Research Professor, Center for Advanced Vehicular Systems, Mississippi State Univ., Mississippi State, MS 39762. Email: particledad@gmail.com

[2]Assistant Research Professor, Center for Advanced Vehicular Systems, Mississippi State Univ., Mississippi State, MS 39762. ORCID: https://orcid.org/0000-0002-2622-4235. Email: bj48@cavs.msstate.edu

[3]Ph.D. Student, Dept. of Civil and Environmental Engineering and Center for Advanced Vehicular Systems, Mississippi State Univ., Mississippi State, MS 39762. Email: ccg228@msstate.edu

[4]CEE Advisory Board Endowed Professor and Associate Professor, Dept. of Civil and Environmental Engineering, Mississippi State Univ., Mississippi State, MS 39762 (corresponding author). ORCID: https://orcid.org/0000-0001-8883-4533. Email: farshid@cee.msstate.edu

[5]Research Professor, Center for Advanced Vehicular Systems, Mississippi State Univ., Mississippi State, MS 39762. Email: mason@cavs.msstate.edu

Note. This manuscript was submitted on October 26, 2018; approved on July 23, 2019No Epub Date. Discussion period open until 0, 0; separate discussions must be submitted for individual papers. This paper is part of the *Journal of Geotechnical and Geoenvironmental Engineering*, © ASCE, ISSN 1090-0241.

The discrete-element method (DEM), which mimics granular kinematics, represents an alternative to continuum-based methods (O'Sullivan 2011). DEM provides a natural approach to granular geologic media by modeling the individual grains. The method has taken a central role in basic research investigating phenomena such as shear localization (Vardoulakis 1980), materials handling (Cleary 2009), fluidization (Kawaguchi et al. 1998), and non-Newtonian fluids (Johnson et al. 2017). A major emphasis of DEM-based research is micromechanics of particle interaction and the relationship of particle kinematics to continuum behavior. This paper considers practical and theoretical aspects of using DEM as an engineering tool for evaluating prototype-scale structures.

This paper gives an example of using a large-scale DEM computer code to model a mobility cone penetration test (CPT). The cone penetration problem was adopted because it represents a difficult numerical problem that has been investigated by many others using experimental, analytical, and numerical methods. Thus, an assessment can be made of the realism of the DEM simulation. The key issues include the suitability of the spherical particle model with rolling resistance to capture macroscale behavior, the ability to calibrate the model using laboratory experiments, the ability to initialize the particle placement within the problem domain with a porosity that represents the relative density of the prototype material, the effect of residual stresses imposed by the initialization technique, and the ability to extract engineering quantities such as stress, strain, and porosity change.

This paper includes a short description of DEM. It is a relatively well-known numerical method, although the method to impose rotational resistance varies among practitioners. The cone problem is introduced along with some typical laboratory results used to evaluate results of DEM simulations. The calibration of DEM is then considered in some detail. Finally, the results of the analysis are presented, followed by a discussion of practical issues that remain to be resolved.

DEM as Engineering Tool

DEM has been used in engineering studies, but to a much lesser extent than for scientific investigations. The principal limiting factor is particle size because it is not feasible to model engineering-scale problems with the same number of particles as are found in the prototype. The steady increase in high-performance computing (HPC) now enables DEM computations with very large particle counts to produce simulations of remarkable levels of realism that have not been available previously (Furuichi et al. 2018). That realism is obtained even though a one-to-one correspondence between a computational particle and a real particle is well beyond reach even with these computational innovations.

Ting et al. (1989) resolved the particle size issue philosophically by noting that DEM is similar to the geotechnical centrifuge in that the number of particles in the model does not approach that of the prototype. The gravity scaling of centrifuge models that allows predictions at prototype scales also increases the scaled particles sizes. The argument for the centrifuge is that, provided the model material has the same constitutive response as the prototype material, the model results give realistic estimates of prototype performance. In the case of the centrifuge, the prototype material is used for the experiment, thus guaranteeing a connection between model and prototype.

However, there are severe limitations to DEM that challenge the centrifuge analogy. In the case of DEM, it is usually not possible to even match the relative grain sizes (Feng et al. 2009). In real soils, grain size can vary by many orders of magnitude, requiring very large numbers of particles for even small soil volumes (Berger and Hrenya 2014). In large-scale studies such as Carrillo et al. (1996), a relatively narrow particle distribution was used; usually a uniformly distributed particle mix, with the smallest particle being one-half the size of the largest particles, was found to be both computationally efficient and obviated the tendency of monosized distribution to crystalize into regular arrays. Unfortunately, while these studies demonstrated the potential for using large-scale DEM in engineering studies, quantitative agreement with physical models was never attempted.

Another issue with DEM is particle shape. For small scientifically oriented studies, there are many approaches to model particle shape realistically. Particles can be described by analytical shapes (e.g., Peters et al. 2009; Cleary and Frank 2006; Kuhn 2003), sphere clusters (e.g., Markauskas et al. 2010; Ferellec and McDowell 2010; Lu and McDowell 2007), and polyhedra (e.g., Hopkins 2014; Nezami et al. 2004). The more complex shapes require more storage, additional computation for particle rotation, more difficult contact detection, and penetration. The amount of additional computational time is somewhat difficult to generalize because the efficiency of the code design must be factored in as well as the fact that nonspherical particles often pack better, thus creating more contacts to be resolved (Kuhn 2003). Kuhn (2003) also found that individual contact computations required six times as long to resolve than for spheres, although the overall computation required only twice as long for the nonsphere versus sphere. Cleary et al. (1997) stated that the time for resolving contacts for smooth shape modeled as a hyperellipse was affected by the aspect ratio of the particle. Nonsmooth polyhedra are more problematic (Nezami et al. 2004), although Hopkins (2014) developed an algorithm that performed 40% as fast as spheres. The additional data required to describe nonsphere geometry can be reduced by selecting shapes from an ensemble that is representative of the granular media (Peters et al. 2009).

Accurate modeling of size and shape can be important for engineering studies in cases where the number of particles is relatively small. For example, in modeling railroad ballast, the particle size is sufficiently large that simulations with a few thousand particles can yield practical results. In such studies, modeling the particles with accuracy is both feasible and critical to accurate prototype behavior (e.g., Ferellec and McDowell 2010; Lu and McDowell 2007).

The problems considered in this paper involve particles that are sand sized or smaller, for which the greater time required for contact detection and penetration computation with nonspherical particles can become onerous when problems involve millions of particles. Using spherical particles offers computational simplicity and efficiency that is essential for simulations with very large particle counts, yet the particle shape is an important factor in replicating the effects of particle rotation. In particular, spherical particles are prone to rolling, giving unrealistic stress-strain results. Tordesillas et al. (2012) noted that a spherical particle can rotate in place without changing the positions of surrounding particles, whereas rotation of a nonspherical particle requires expansion of the assemblage. This geometric feature implies that nonsphericity has a role in volume change behavior. It is not clear that this simple example applies when rolling resistance is added to the contact behavior because rolling resistance also affects force chain instability, which also contributes to volume change (Tordesillas et al. 2009). Tordesillas et al. (2009) also documented the importance of force chain instability to affect shear band formation. In assemblages of spheres, volume change and shear banding are both linked to rolling resistance and are key indicators of model accuracy. A detailed three-dimensional analysis of pile jacking by Zhang and Wang (2015) likewise used spherical particles with rolling resistance.

Given these limitations in capturing the particle-scale attributes with fidelity, the use of DEM for engineering studies comes down to one fundamental issue: can the parameters used to model particle-scale behavior be chosen to obtain realistic engineering-scale behavior? Implicit in this question is that there is not a unique relationship between the microscale model and the macroscale response. Thus, although the macroscale behavior can be captured by accurately modeling microscale properties, it can also be modeled to differing degrees of accuracy by a large number of microscale representations that are significantly simplified. It follows that it might be possible to create a microscale response using spherical particles, stabilized with rotation resistance, that reproduces a macroscale response that is sufficiently accurate for prototype-scale engineering analyses. Given such an effective response media, the particle size becomes a parameter used to control mesoscale effects such as force chain length or shear band thickness, both of which are measured in terms of number of particles (e.g., Mühlhaus and Vardoulakis 1987; Peters et al. 2005). The Ting et al. (1989) proposition becomes valid provided there is sufficient resolution, as measured by the particle size relative to the problem domain size.

Discrete-Element Method

DEM (Cundall and Strack 1979) is a numerical model for simulating the behavior of granular particle assembly by tracking the motion of each individual particle. Particles interact through forces computed from empirical contact laws. The motion of each particle is dictated by a sum of body forces and contact-induced forces and moments. Contact forces and moments follow contact laws that represent physical interactions between realistic particles. The DEM code used was developed at the US Army Engineer Research and Development Center (ERDC) for the prototype-scale analyses described in this paper. It is a straightforward application of high-performance computing with message-passing interface (HPC-MPI) techniques that can easily deal with particle-scale resolutions requiring more than 10 million particles. Thus far, the code has been used for simulations of up to 93 million particles using 3,384 processors.

DEM is a procedure for simulating interacting bodies through integration of the equations of motion for each body. The forces caused by interactions are computed using binary contact laws based on the relative movement between the bodies at the point of their contact. The bodies themselves are assumed to be rigid, with the contact deformation idealized as a small interpenetration at the contacts. To simplify contact detection for large-scale problems, particles are assumed to be spherical, but not necessarily of equal size. Interactions between particles are described by contact laws that define forces and moments created by relative motions of the particles. The motion of each particle that results from the net forces and moments are obtained by integrating Newton's second law. Thus, the particles are not treated as a medium. Rather, the continuum behavior *emerges* from the interactions of the particles comprising the assemblage (Cundall and Strack 1979; Cundall 2001).

The evolutions of particle velocity v_i and rotational rate ω_i are given by

$$m\frac{\partial v_i}{\partial t} = mgn_i^g + \sum_{c=1}^{N_c} f_i^c \tag{1}$$

and

$$I_m\frac{\partial \omega_k}{\partial t} = \sum_{c=1}^{N_c} e_{ijk} f_i^c r_j^c + \sum_{c=1}^{N_c} m_k^c \tag{2}$$

where m and I_m = particle mass and moment of inertia, respectively; gn_i^g is the acceleration of gravity vector; f_i^c and m_k^c = forces and moments applied at the contacts; r_j^c is the vector from the particle center to the contact location; and N_c = number of contacts for the particle. A repeated subscript implies summation in the usual fashion except where otherwise stated.

Contact Laws

Particle forces are accumulated from pairwise interactions between particles referred to as a contact. The nomenclature for particles in contact is shown in Fig. 1. Capital letters A and B are used to denote members of a contacting particle pair. When a quantity is denoted as a vector or tensor component using index notation, the member in denoted by a superscript; otherwise it is denoted by a subscript. By this nomenclature, two particles with radii R_A and R_B make contact when the distance, d, separating the particles satisfies

$$d < R_A + R_B \tag{3}$$

A similar rule applies for contact between particles and the triangular facets used to model the surface of rigid objects such as the cone (Horner et al. 1998).

Interactions between particles are described by contact laws that define forces and moments created by *relative* motions of the particles. The motion of each individual particle is described by the velocity of the particle center and the rotation about the center. The branch vector between particle centers $x_i^A - x_i^B$ is also the difference between the respective radii vectors that link the particle centers to the contact $r_i^A - r_i^B$. With this nomenclature, the relative motion at contact c between particles A and B is given by

$$\dot{\Delta}_i^c = \dot{u}_i^A - \dot{u}_i^B + e_{ijk}(r_j^A\omega_k^A - r_j^B\omega_k^B) \tag{4}$$

where $\dot{u}_i^A$ and $\dot{u}_i^B$ = velocities of particles in contact; and e_{ijk} = permutation symbol. The contact moments are generated by the difference in rotations, $\Delta\theta_i^c$, between the particles

$$\Delta\theta_i^c = \Delta t(\omega_i^A - \omega_i^B) \tag{5}$$

The contact forces for cohesionless materials are given by the contact laws in terms of their normal and shear components, f^n and f_i^s

$$f^n = \begin{cases} K^n\Delta^n \\ E_r K^n(\Delta^o - \Delta^n), \quad \Delta^n < \Delta^o \end{cases} \tag{6}$$

$$f_i^s = \begin{cases} K^s\Delta_i^s \\ f^n \tan\phi n_i^s, \quad |f_i^s| \geq f^n \tan\phi \end{cases} \tag{7}$$

and the contact moment

$$m_i^c = \begin{cases} K^m\Delta\theta_i^c \\ f^n \tan\phi_m n_i^m, \quad |m_i^c| \geq f^n \tan\phi_m \end{cases} \tag{8}$$

where K^n, K^s, and K^m = normal, shear, and rolling stiffness constants; E_r = factor to create an energy-dissipating hysteresis loop through stiffening the unload response; Δ^n and Δ_i^s = normal and shear components of the contact displacement; n_i^s and n_i^m are unit vectors in the direction of the shear force and moment; Δ^o = greatest value of penetration in the history of Δ^n; and ϕ and ϕ_m = friction parameters. Eq. (6) was introduced for damping particle interactions in the normal mode by Walton and Braun (1986). Damping is also implicit in the friction laws in the sliding and rotational modes. Viscous damping is also included within the unload-reload segments of the hysteretic damping of Eq. (6). The unload-reload segment is elastic, which can give rise to undamped vibrations. To reduce these vibrations, a viscous damping parameter is computed as $0.1\sqrt{mE_rK^n}$. This viscous damping is restricted to contacts in the unload-reload portions of the contact laws.

The time step $\Delta t = 2.06 \times 10^{-7}$ s is the time step for integration of Newton's law, a value roughly one-tenth the critical value as computed from the smallest mass and stiffest contact spring. The mass used in Eq. (1) is the same as the actual soil particles. Our experience is that although increasing the inertia increases the critical computational time step, it also reduces the wave speed, which in turn can cause problems with the response to imposed loads. In effect, the rate of loading also has to be slowed, leading to a

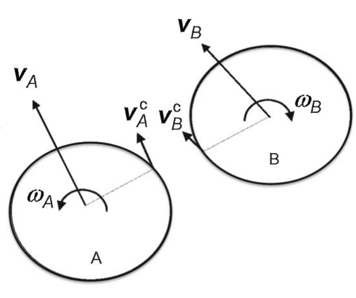

F1:1 **Fig. 1.** Numbering system for two particles in contact.

total computational time not much different than required using the real mass.

Calibration

Despite the simplicity of the contact laws, the general shape of the stress-strain curve and the shear volume change behavior observed in soil are captured well *qualitatively* as an emergent macroscale feature (Goodman et al. 2017). Calibration of the contact properties is needed to obtain reasonable *quantitative* agreement with macroscale behavior. The particle size is selected to be small enough that mesoscale features such as force chains do not affect results, yet large enough to keep the particle count within a practical range. The competing criteria are similar to those considered in finite-element analyses.

In principle, parameters controlling normal and shear response at the contact can be determined from independent experiments on particle pairs (e.g., Cole and Peters 2007). Although such an approach is valid for DEM applied to micromechanical studies in which the particle shapes and size distribution are realistically modeled, for prototype studies the particle interaction parameters are instead estimated to give the best macroscale response. In particular, a microscale measurement is not possible for determining the properties of the exaggerated rotational contact stiffness required to stabilize spherical particles. Rotational resistance requires a calibration motivated solely by the macroscale response [i.e., bulk calibration of Coetzee (2017)].

Parameters controlling contact behavior were determined from a parametric study using simulations of a standard laboratory plane strain test such as described by Alshibli and Sture (2000) (Tables 1 and 2). Reasonable values for the normal and shear stiffness were relatively straightforward whereby they were related to the initial stiffness of the plane strain specimens. As the stress-strain curve became increasingly nonlinear, the sliding resistance and rolling resistance became more critical. A series of simulations were performed in which $\tan\phi$ and $\tan\phi_m$ were varied until stress-strain behavior similar to that of experimental plane strain tests was achieved. The realism of the fit was based on a qualitative comparison to the experiment of simulated stress-strain curve shape and the peak strength.

Unfortunately, the combination of rolling and sliding friction that give a specified peak strength is not unique because many pairs of these parameters can render the same peak strength. To get a unique calibration, the parameter pair should be coupled with a pair of macroscale quantities to complete the comparison. Rather than focus on a particular parameter, the choice of rotational resistance was based on what gave the best representation of the shear band formed at failure. The rolling resistance has significant influence on particle rotations associated with shear band formation and volume change within the band. When the rolling resistance is zero shear, band formation is not resisted, with the result that the shear band intersects the corner of the walls of the apparatus. Thus, it appears that the specimen geometry controls the shear band orientation when rolling resistance is zero. In the case of $\tan\phi_m > 0.1$, the particle rotations that accompany shear localization were inhibited and no shear band formed. Realistic shear bands (e.g., Fig. 2) formed in the parameter range of $0.1 > \tan\phi_m > 0.01$. Within this range, rotations of the individual particles varied as axial strain increases throughout the course of the simulation. The rotations were initially scattered throughout the specimen, but eventually localized along with large dilatational strain within the shear band. Once formed, the localized rotations carried on throughout the remainder of the simulation.

Table 1 shows the relavent details for calibration of DEM in comparison with the plane strain experiments of Alshibli and Sture (2000). For the aspect ratio, half the width perpendicular to the plane strain face was modeled for computational efficiency. Also, the peak principal stress ratios for DEM were found only by changing rolling resistance and sliding friction at the particle contacts, while the range given from the physical experiments was found by varying confining pressure. Further research on the coupled effects of confining pressure and particle contact frictions is needed. The parameters chosen for this analysis are assumed appropriate for the shallow penetration depths of a few centimeters.

Table 1. Comparison of the data from the plane strain experiment (Alshibli and Sture 2000) with the current DEM calibration

Property	Alshibli and Sture (2000)	DEM
Sample aspect ratio (height:length:width)	~2:1:1	2:1:0.5
Peak principal stress ratio (σ_1/σ_3)	5.0–7.5	4.2–7.5
Shear band inclination[a]	53°–57°	57°–60°
Confining pressure (kPa)	100	70
Porosity	0.33–0.45[b]	0.37

[a]Observed at approximately 10% strain.
[b]Obtained from minimum and maximum void ratio (Table 2).

Table 2. Properties of the sands used for the plane strain [reported by Alshibli and Sture (2000)] and mobility cone [reported by Melzer (1971)] tests

Property	Melzer (1971) Bayou pierre sand	Alshibli and Sture (2000) F-75 Ottawa sand
e_{min}	0.410	0.482
e_{max}	0.658	0.805
d_{50} (mm)	0.46	0.22
G_s	2.65	2.65
D_r (%)	97	97
C_c	1.03	1.00
C_u	2.5	2.0

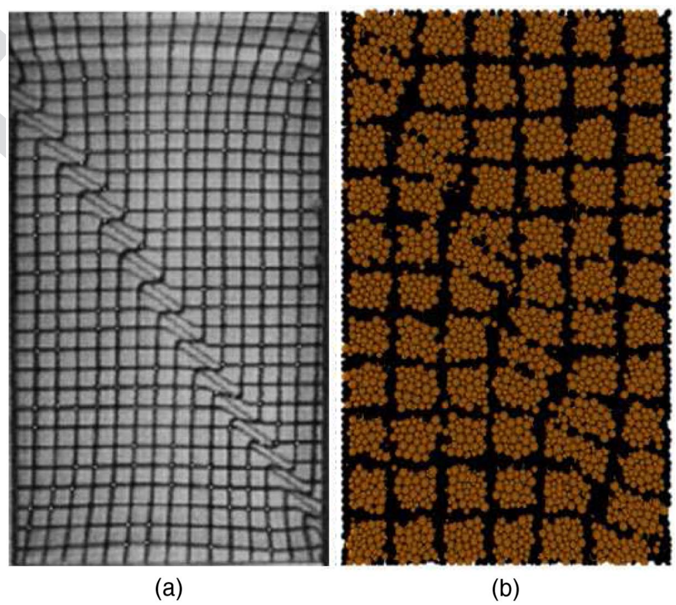

Fig. 2. Comparison of shear band patterns for (a) Alshibli and Sture's (2000) experiments; versus (b) DEM simulations. [Reprinted (a) from Alshibli and Sture (2000), © ASCE.]

The problems associated with modeling the grain size and grain shape also affect the ability to model particle porosity. The porosity is a major factor affecting engineering behavior. However, what is dense versus loose depends on particle size distribution and shape (Salot et al. 2009). If these particle attributes are not the same in model and prototype, the relationship between porosity and engineering behavior will likewise differ in the model and prototype. Thus, part of the calibration must include a determination of what porosities constitute loose versus dense states for the computational particles and how that porosity relates to that of the prototype soil. Although porosity is a macroscale measure of soil state, Knuth et al. (2012) noted that strength depends on the number of contacts, not merely porosity. This dependence on the number of shared contacts suggests a microscale state parameter could be developed based on coordination number rather than porosity, a possibility not considered here.

Example Analysis

Simulations of the so-called mobility cone (Melzer 1971) will be used to illustrate the key principles in prototype-scale analyses. The mobility cone is a handheld device shown in Fig. 3, with dimensions in Table 3, that is intended to evaluate terrain details based on

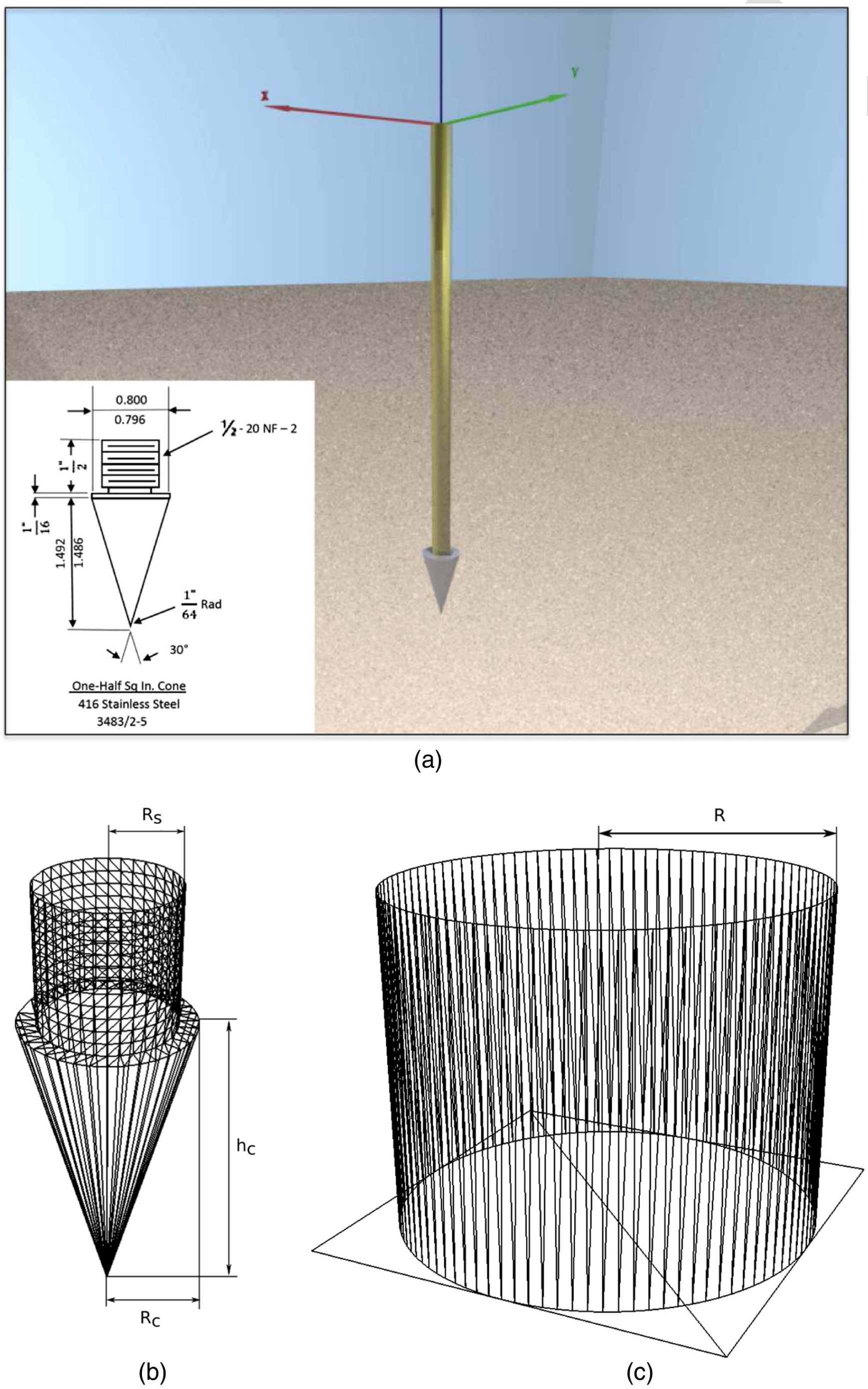

Fig. 3. (a) Mobility cone with insert, with details in US customary units; (b) triangular facet representation of a probe; and (c) cylindrical calibration chamber.

Table 3. Dimensions of the probe and mold in the cone penetrometer test

Property	Symbol	Units	Value
Cone radius	R_c	cm	1.02
Cone height	h_c	cm	3.79
Cone angle	α	degrees	30.00
Shaft radius	R_s	cm	0.80
Mold radius	r	cm	19.0

Table 4. Material properties used in the DEM simulation of the mobility cone penetrometer test

Property	Symbol	Units	Value
Specific gravity	G_s	—	2.65
Particle–particle			
Normal stiffness	K^n	kN/m	245
Hysteretic unload-reload ratio	E_r	—	1.1
Shear stiffness	K^s	kN/m	87.6
Contact friction (sliding)	$\tan \phi$	—	0.50
Rolling stiffness	K^m	Nm/rad	56.5
Contact friction (rolling)	$\tan \phi_m$	m	0.01
Particle–wall			
Normal stiffness	K^n	kN/m	210
Hysteretic unload-reload ratio	E_r	—	1.1
Shear stiffness	K^s	kN/m	0.00
Contact friction (sliding)	$\tan \phi$	—	0.20
Rolling stiffness	K^m	Nm/rad	56.5
Contact friction (rolling)	$\tan \phi_m$	m	0.00

the cone index (CI). It is the basis of a rapid mobility assessment procedure (Priddy et al. 2012). The key measurable quantity for the mobility cone is the cone index, which is the force measured at the surface divided by the cone area. Given that the cone tip is larger than the shaft (Fig. 3) and considering the shallow depths for which the mobility cone is used, the cone resistance is primarily the total force on the cone tip. The purpose of the analysis is to relate the tip resistance to engineering properties such as stiffness and strength parameters as well as the soil density state. The process involves first computing the stress state imposed by the advancing cone. The tractions acting on the cone face are then integrated to obtain the total vertical force. For the mobility cone, empirical relationships are used to predict vehicle traction from cone resistance based on extensive field tests.

From a historic perspective, the mobility cone penetrometer was adopted by the US Army in the mid-1940s from the North Dakota Department of Transportation, where it was used to evaluate unimproved roads. The mobility cone penetrometer was a simple and effective method for measuring the bearing capacity of the soil and is the primary method used by the US Army for evaluating off-road mobility (Stevens et al. 2013). During the early years, a comprehensive study by Melzer (1971) evaluated a variety of sand types relating mobility cone penetration measurements in the laboratory under controlled conditions with respect to density, gradation, and mean grain size diameter. The study suggested for a tire operating on a medium to loose sand, the depth of interest was from the surface to 15 cm. The Melzer data were documented in enough detail to support the validation of the DEM efforts in this study without additional laboratory testing. Table 2 compares the sand used for calibration (Alshibli and Sture 2000) with the sand tested by Melzer (1971). The principal basis of comparison between the sands used by Alshibli and Sture (2000) and Melzer (1971) was the relative density.

Comparison of Numerical Methods

Traditional analysis of the cone penetration mechanics includes cavity expansion theory and limit analyses (e.g., Yu and Houlsby 1991; Salgado et al. 1997; Ahmadi et al. 2005; Mayne 2006; Gui and Jeng 2009).

The finite-element method provides a better characterization of the cavity expansion process whereby the penetration is treated as a prescribed displacement in the shape of the advancing cone. When applied to the cone cavity expansion, the cone's insertion is envisioned as cylindrical cavity with a virtually zero initial radius that is expanded to the ultimate cone radius. Effectively, the probe insertion is modeled by prescribing displacements along a preexisting line of elements that marks the center of the cone advance (Kiousis et al. 1988; Abu-Farsakh et al. 1998; van den Berg et al. 1996; Huang et al. 2004; Markauskas et al. 2002; Jarast and Ghayoomi 2018). Abu-Farsakh et al. (1998) especially illustrates the power of the finite-element-based cavity expansion because the pore pressure imposed by penetration can be included in the analysis. Importantly, these analyses depend on the preexistence of a cavity that can be expanded. Analyses using sophisticated constitutive models and advanced large-deformation modeling were presented by Jin et al. (2018) and Fan et al. (2018).

DEM requires no assumption on the continuous nature of the motion, nor are there problems created by singularities caused by the geometry of the cone tip. The method has been applied to the cone problem using small particle counts on the order of 100,000 particles or less. Two-dimensional studies of granular media using DEM were performed by Jiang et al. (2008). In three-dimensional studies (Butlanska et al. 2013; Falagush et al. 2015), the particle count was kept relatively small through adept use of modeling techniques that took advantage of the problem's axisymmetry and using multiresolution. A three-dimensional study of a cone penetrometer was performed by Kotrocz et al. (2016) based on using DEM calibrated to a direct shear box. A high degree of noise appears to be characteristic of these analyses, possibly because of the small number of particles used in each case [see also Arroyo et al. (2011) for a description of noise in the cone force record caused by large particle sizes]. Holmen et al. (2017) presented results for penetration of hemispherical-, blunt- and ogival-shaped impactors from simulations using 0.5×10^6 to 3.2×10^6 particles. Although the larger models required significantly greater computation time, the smaller models apparently imposed greater penetration resistance.

Problem Description

The material properties and dimensions for the cone simulation are listed in Tables 4 and 5. Fig. 4(a) shows a cutaway view of the model after partial cone penetration. The particles are placed within a cylindrical mold to a specified density. In the simulations, the particle density was obtained by either sedimenting under gravity or applying an additional compaction loading applied to a metal plate. The metal plate was also used to apply a surcharge loading to simulate conditions at greater depths. The physical tests by Melzer (1971), used herein for comparison, did not include the surcharge loading case. The size of the test cylinder matched that used in the physical tests by Melzer (1971).

The cone with radius R_c was assumed to be advanced into a laboratory testing cell with radius $R = 19$ cm. The total soil height was Z. Initially, the cone sat above the cell without contact with the soil. At the testing cell outer boundary, the horizontal displacement was zero ($u_r|_{r=R} = 0$). The vertical movement was impeded only

Table 5. Parameters of particle samples in the DEM simulation of CPT and in the experiment used for calibration

			Values			
Property	Symbol	Units	Experiment	DEM 1×	DEM 2×	DEM 4×
Particles						
Number	N	—	—	9,504,976	4,828,755	2,385,295
Minimum diameter	$d_{\min}$	mm	∼0.05	0.74	0.89	1.24
Mean diameter	d_{mean}	mm	0.50	1.62	2.03	2.56
Maximum diameter	$d_{\max}$	mm	∼8.00	2.16	2.74	3.42
Settled sample						
Initial specimen height	z	cm	30.0	31.3	—	—
Initial mean porosity	n	—	0.30	0.40	—	—
Compacted sample						
Initial specimen height	z	cm	30.0	29.8	30.2	30.0
Initial mean porosity	n	—	0.29	0.37	0.38	0.37
Compacted sample with surcharge						
Initial specimen height	z	cm	—	29.7	—	—
Initial mean porosity	n	—	—	0.37	—	—
Confining pressure	p	kPa	—	115[a]	—	—

[a]Confining pressure was only applied in CPT simulation with overburden surcharge. Remaining CPT simulations did not impose confining pressure.

by the soil–container friction. At the bottom boundary the vertical displacement was zero ($u_z|_{z=0} = 0$) and the horizontal movement was impeded by the soil–container friction.

Sample Initialization

The principal difficulty with sample initialization is placing the large number of particles within the problem boundary in static equilibrium, such that a target density is obtained. The initial porosity and stress should be checked by high-resolution postprocessing methods to assess homogeneity in porosity and residual stresses created by compaction methods used.

The initialization steps include initial placement, settling under gravity, and external forces to reach equilibrium, subsequent to compaction to obtain the desired density. For simple domain shapes, simulated compaction can be applied to decrease the initial porosity, although this also introduces residual compaction stresses, possibly requiring an additional relaxation step in which domain boundaries are expanded by some small amount.

The settling step can be time-consuming unless the initial placement is close to the desired final placement. The initial particle configuration for the DEM simulation described here was obtained from a presettlement iterative procedure that is independent of DEM. In this preprocessing procedure, the interior of the test mold was filled with a tetrahedral mesh using the meshing package TetGen. The tetrahedral mesh facilitated an iterative procedure that tightly packs the particles. Spherical particles were placed at element centers and nodes of the tetrahedral mesh with diameters somewhat smaller that the target diameters. The iterative algorithm adjusted particle locations and increased sizes while keeping particle contacts in a near-touching state such that no interparticle forces were induced. The tetrahedral mesh was not a part of the subsequent DEM computations.

After this initial placement, one of two sample configurations were prepared using the DEM algorithm: settled and compacted. The settled sample was placed under gravity loading only. The compacted sample was first settled and then compacted by a surcharge loading at the surface applied by a plate moving at constant velocity. Compaction was followed by unloading and removing the surcharge plate to produce a gravity-loading condition. Higher densities were achieved by imposing overburden pressure. The most effective method to achieve higher densities was to set the contact frictions to zero during the settling phase. Other than that, the contact parameters were not adjusted to achieve the higher density. Thus, the interparticle friction was specified as zero during the compaction phase to facilitate densification. The computations were continued until the desired compaction was achieved, at which point some small particle motion remained. The contacts were then assigned friction values and additional computational steps were taken until the sample reached equilibrium. These friction parameters were then used for all subsequent simulation steps.

To investigate the effect of confining stress on cone performance, a second set of simulations was performed with a surcharge load applied equivalent to 6.1 m of overburden, corresponding to an external pressure of 115 kPa. The surcharge was created by applying a vertical load through a plate placed on top of the specimen. The mobility cone does not penetrate to such depths; these simulations were intended to test effects of higher stress in principle.

Parallel Partitioning and Performance

The present DEM implementation was parallelized by *particle partitioning*, which is a parallelization scheme that distributes the particles among processors [Fig. 5(a)]. Each processor only updates the states of its own particles and each particle stays with the same processor throughout the whole computation. Information about neighboring particles is communicated between processors using MPI library calls. Alternatively, the space can be divided into subdomains for individual processors, leading to *space partitioning* [Fig. 5(b)]. In this parallelization scheme, a particle will be moved to another processor when it enters the spatial subdomain belonging to another processor. In Fig. 6, parallel speedup of the present code, which uses particle partitioning, is evaluated and compared with the space partitioning as implemented in the LIGGGHTS DEM package. Parallel performance was measured on a Topaz supercomputer (SGI ICE X system at US Army Engineer Research and Development Center, Vicksburg, Mississippi) using the nodes with two 18-core Intel (Santa Clara, California) Xeon E5-2699v3 processors and 116 GB of RAM. The benchmark examined settling of 9.5 million particles under gravity over 50,000 time steps. The faster of two benchmark executions using a single core of Topaz took 59 h 2 min. As seen in Fig. 6, DEM with particle partitioning performs better with a low number of MPI processes, whereas space partitioning is advantageous for a large number of MPI processes, where the particle partitioning curve exhibits a noticeable decrease in slope.

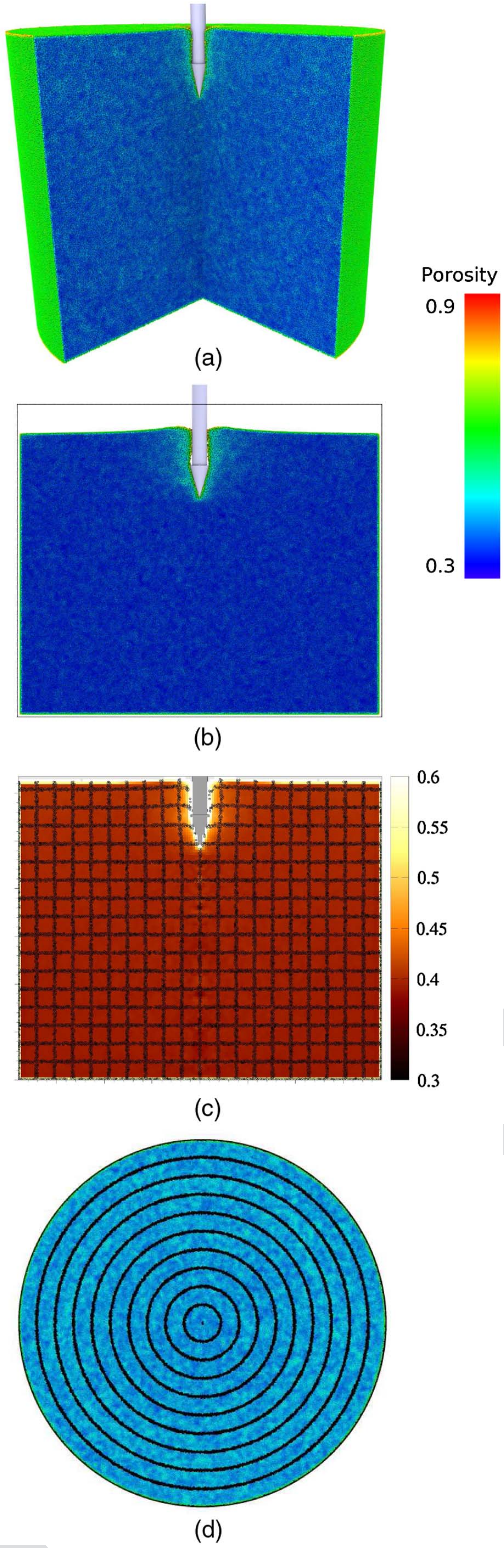

Fig. 4. (a) Cutaway view of experimental setup; and (b) section view. (c) The particle quantities can be shown by averaging quantities in the circumferential direction, where selected particles are colored black to create a material grid. (d) The vertical view gives a direct observation of the cavity expansion process within a particular plane.

Layout of Results

Results from the simulation can be shown in various formats as illustrated in Fig. 4. The quantity of interest—porosity in this illustration—is depicted by coloring the particles. A section view is shown in Fig. 4(b). Although the analysis was fully three-dimensional, the behavior closely approximated axial symmetry, making the section view a relatively complete graphical description of the behavior. The section view in Fig. 4(c) is also effective for illustrating axisymmetric averages computed from particle values within circumferential cells. Interpretation is aided by adding a material grid. The grid is created by marking particles originally within the vicinity of initial axisymmetric grid lines. Inasmuch as the grid particles follow the motion of the individual grains, they approximate a *material grid*. The same averaging technique and grid can be used to create a vertical view as shown in Fig. 4(d).

Cone Action and Penetration Resistance

The probe was inserted into the sample with a constant velocity of 3.05 cm/s. As the depth of the cone increased, the resistance of the sample increased. Cone penetration resistance, also referred to as *CI*, was obtained by dividing the vertical force acting on the probe by the cross-section area of the cone

$$CI = \frac{F_z}{A_c} = \frac{F_z}{\pi R_c^2} \tag{9}$$

Fig. 7 shows the resulting cone penetration resistance, compared with Melzer (1971). The general trend of the cone resistance is similar to the laboratory results. The high resolution of the simulated plot reveals some variation in cone index caused by heterogeneity of the simulated medium that is not seen in the lower resolution laboratory results. The friction coefficient between the soil and metal, denoted WF in the plot, clearly affects the cone resistance with $\mathrm{WF} = 0.3$, causing a cone resistance that is approximately 33% higher than with $\mathrm{WF} = 0.2$. Unfortunately, the cone–soil friction was not measured in the laboratory experiment nor is it generally available in field measurements.

The effect of the DEM particle size is demonstrated by measuring cone penetration resistance for two samples with larger particles. The number of particles in these coarser configurations, as listed in Table 5, was approximately two and four times smaller than the number of particles in the finest sample. Contact parameters for samples with larger particles were adjusted in accord with mean particle radius to maintain the same bulk stiffness. The recalibration of the particle stiffness is needed because the contact law introduces a size dependency in the contact force law (see also Holmen et al. 2017). The friction values were specified as zero during the settling phase. As expected, the response from configuration with four times fewer particles is less smooth than the responses from configurations with finer particles. Importantly, the response from configuration with two times fewer particles is close to the response from the finest configuration, showing that the process of refining particle size has converged.

Particle Kinematics

Fig. 8 shows a deformed grid view of the cone advancement. The grids shown in Fig. 8 are similar to experimental result shown in Fig. 2 of Ahmadi et al. (2005). In the context of continuum mechanics, the material grid has the important characteristic of defining affine motion of the media. Under such deformation, particles that are neighbors remain neighbors, thus maintaining the topology on the contact network. The particles only approximate affine deformation with their movement containing some diffusive movement, although the approximation to continuum motion appears good when viewed at the scale of the grid size.

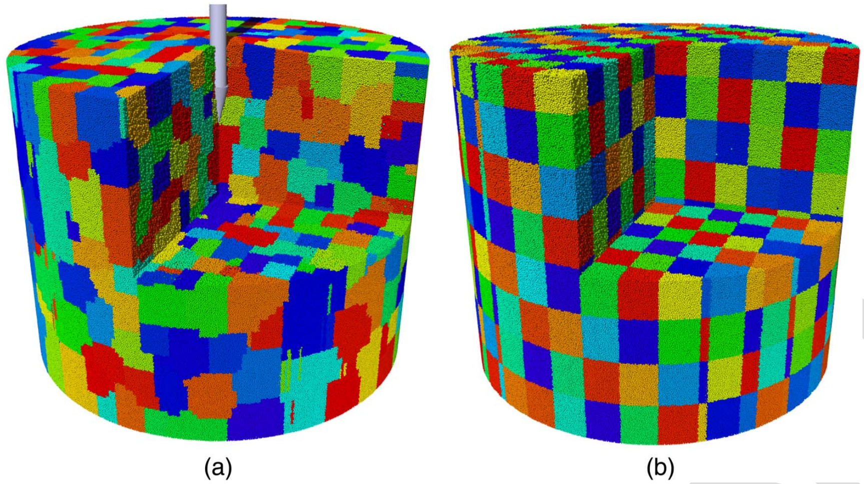

Fig. 5. Processor assignments. Colored regions represent particles assigned to the same processor for (a) particle partitioning; and (b) space partitioning.

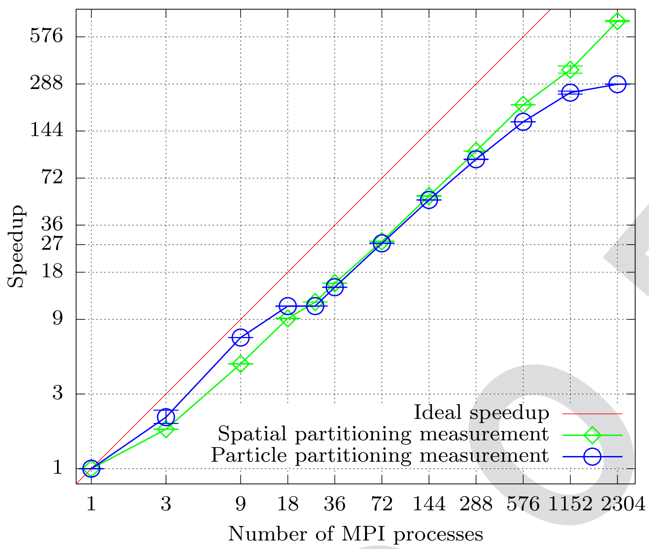

Fig. 6. DEM speedup plot with particle and space partitioning. Range of two measurements at each number of MPI processes is indicated by horizontal bars.

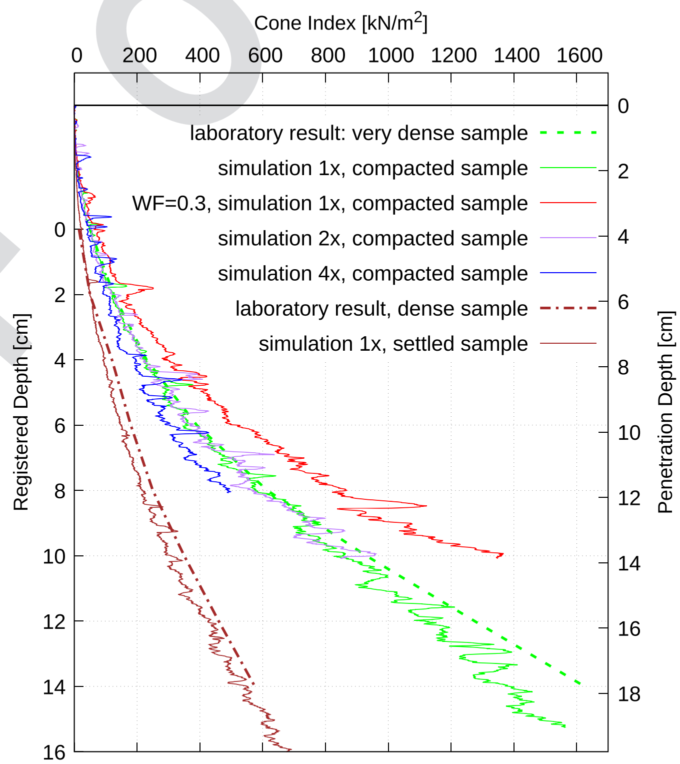

Fig. 7. Cone index versus depth for two levels of particle densifications compared to typical laboratory results. WF indicates the friction coefficient between the cone and soil.

Horizontal Displacement

The history of horizontal displacement is shown in Fig. 9, which depicts the passage of the cone through a selected horizon. Although the cavity expansion theory is best based on a spherical cavity (Yu 2006), what is depicted in this figure and elsewhere is a cylindrically shaped opening. Four cases are shown, allowing comparison when initialization is done by settling or compressing and with and without surcharge. Each case shows a sequence of four stages of cone advance, with the initial state shown in the upper left quadrant for each case and the three subsequent scenes shown arrayed in a clockwise order. For cases with surcharge, a horizontal plate with mass of 1,330 kg exerting a pressure of 115 kPa was placed on the top surface. The combined effect of stress and porosity can be seen clearly by comparing the cases. The porosity increased in all four cases. The relative displacement of grid lines (indicated by apparent displacement in grid lines between quadrants) indicates that the effect of cavity expansion was greatest for the settled specimen without surcharge. The greatest porosity increase was observed for the settled case without surcharge, presumably because the initial loose state allowed greater deformation. A similar deformation was seen for the case with surcharge. The compressed specimen had the least horizontal grid displacement and smallest porosity change.

Displacement Velocity

Fig. 10 shows average particle velocities. The velocities were averaged over 76×120 axially centered concentric rings. The arrows

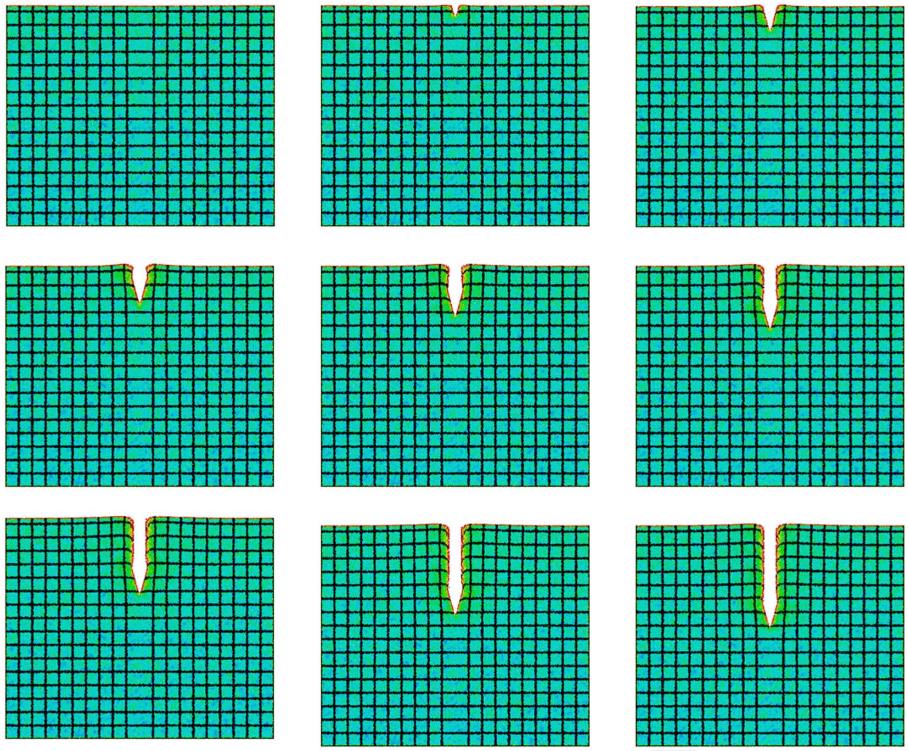

Fig. 8. Material grid deformation as penetration proceeds.

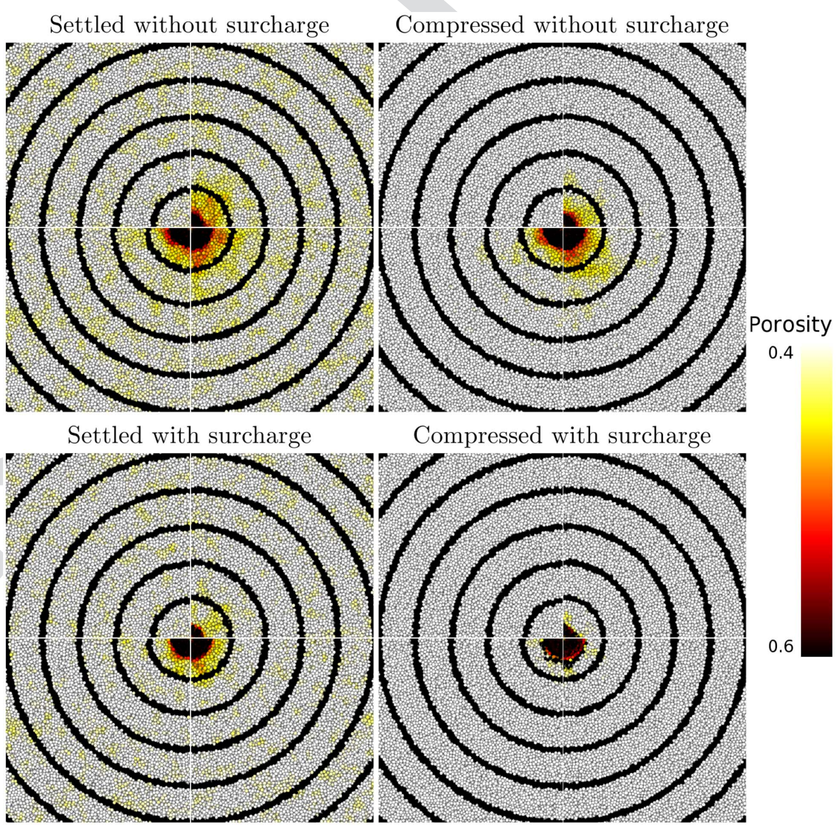

Fig. 9. Vertical views for four cases: settled and compacted samples, each with and without surcharge. Each case is broken into quadrants showing different cone position (as indicated by black coloring in the center). Particle coloring indicates local porosity. Sequence of time snapshots within cases progresses in a clockwise direction.

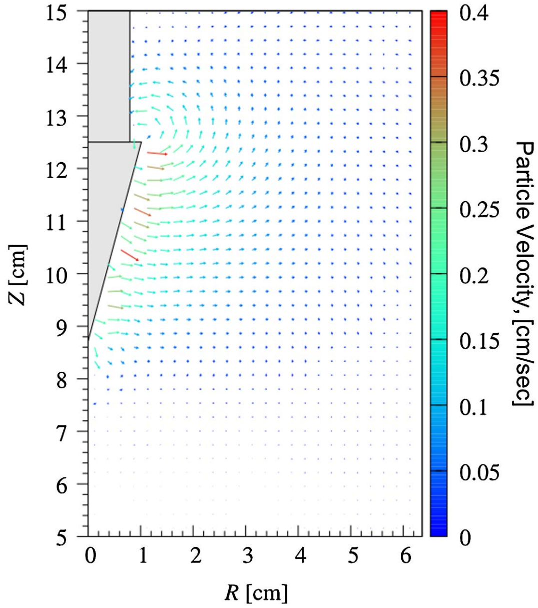

Fig. 10. Velocities of particles. Color represents magnitude in centimeters per second.

representing the velocity vectors start in the updated particle location. Along the cone sleeve, particles move in the direction perpendicular to the cone surface away from the cone. Just about the cone collar, where the shaft starts, the particles start moving backward with a vortex motion toward the shaft, into the void created by the reduced shaft diameter.

At shallow penetration, the particles along the shaft moved in the downward direction along with the probe, with velocity much lower than the probe velocity. The largest particle velocity was observed near the cone tip in the compacted sample. The magnitude of particle velocities in the cone tip region approached the velocity of the probe.

632 Porosity

Local porosity n^p represents the void volume fraction within a selected spherical neighborhood surrounding each particle. It was evaluated as

$$n^p = 1 - \frac{V_S}{V_T} \tag{10}$$

where V_T = total volume of the sampling spherical neighborhood of the particle p; and V_S = volume of the particles (solids volume) within the neighborhood. A sampling radius, R_N, that is three times the radius of the largest particle was found to give a representative local porosity based on test cases of particle assemblages fabricated to have known porosity. Where portions of a neighboring particle extends beyond the sampling sphere boundary, its contribution to the solids volume is computed as the intersection volume of the particle and sphere given by

$$V_\cap = \frac{\pi(R_N + r_p - d)^2(d^2 + 2d(R_N + r_p) - 3(R_N - r_p)^2)}{12d} \tag{11}$$

where d = distance between the sphere and particle centers; and r_p = radius of the particle p.

Snapshots of averaged porosity during the cone penetration within the settled and compacted samples are shown in Fig. 11. Starting from the undisturbed sample with initial porosity of 0.37, the plot in Fig. 11 shows an increase in porosity as the probe advances. Importantly, the porosity increases even in the high-stress region around the cone tip. Consider a cylindrical-shaped volume created by the grid cells introduced in Fig. 4. A close inspection of any of the grid cells shows that the particles closely follow material deformation paths. As noted previously, the solids volume thus remains constant as the grid cell deforms. The cylindrical-shaped grid cells are expanded as the probe passes (cavity expansion), causing their total circumference to increase. If the thickness of the expanded cylindrical cells stays relatively constant, as in the case considered here, the result will be an increase in cell volume causing a porosity increase.

As seen in Fig. 11, the application of overburden stress reduces the volume expansion significantly, suggesting greater compressibility of the particle domain under higher initial stress. This effect is fully consistent with observed soil behavior, although it should be recognized that there is nothing in the contact laws that makes the particle interactions more compliant at higher stress levels. To understand the effect of higher confining stress on volume change, a broader analysis is needed that is beyond the scope of the present paper.

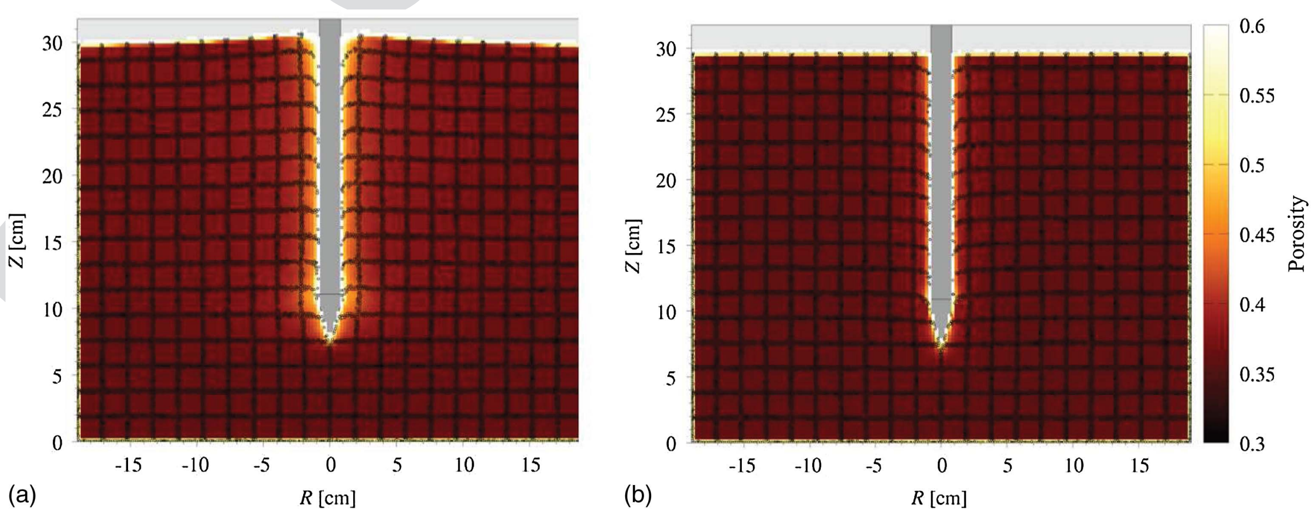

Fig. 11. Averaged particle porosity for a compacted specimen with (a) no overburden surcharge; and (b) overburden surcharge.

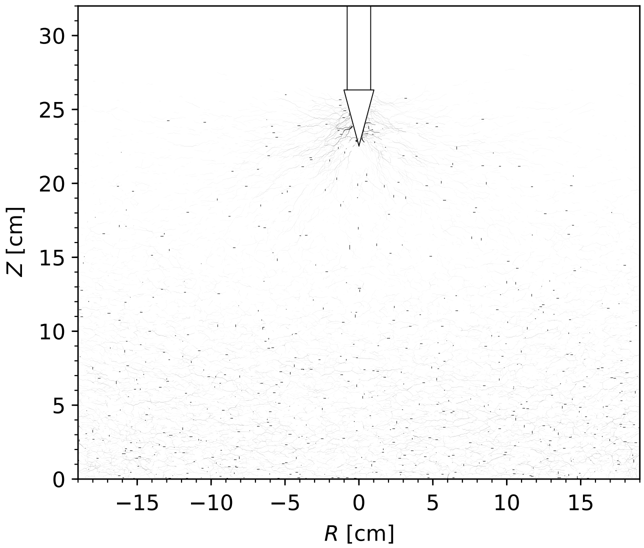

F12:1 **Fig. 12.** Pairwise contact forces between particles.

Average Particle Stress

Various macroscale quantities of interest to engineering interpretation can be computed from averaging particle and contact quantities. The microscale counterpart of stress is the contact force. The macroscale stress is an average of the contact forces as will be discussed subsequently. However, before considering the macroscale quantity, the microscale contact force will illustrate the changing stress anisotropy as inferred from the major contact force directions. The contact forces shown as force chains in Fig. 12 reveal a discrete force chain characteristic of granular media. Only the forces near the specimen midsection with magnitudes larger than a chosen threshold are displayed. The threshold value is 0.044N at $t = 2.4$ s and 0.44N at $t = 7.4$ s. The magnitude of contact force is indicated by the thickness of the line connecting particles in contact. The stress bulb imposed by the cone tip is clearly expressed by the intensity of the chains. Also apparent is the changing directionality as the forces propagate from the cone tip. This pattern is relatively constant as the cone advances, especially in the settled case. In the compacted case for shallow depths, the residual horizontal stress somewhat masks the trend, although as the cone advances deeper the forces associated with the cone overwhelm those associated with the residual compaction stress.

The particle stress is a quantity computed for each particle based on the contact forces

$$\sigma_{ij}^{p} = \frac{1}{V_P} \sum_{q=1}^{N_c} r_i^{pq} f_j^{pq} \tag{12}$$

where V_p = volume of the particle p; $r_i^{pq} = i$th component of the vector r that connects the particle center to the contact, which for spherical particles lies in the direction of the vector connecting centers of particles p and q; $f_j^{pq} = j$th component of a contact force between the two particles; and the sum is performed over the number of contacts N_c of the particle p.

Components of average horizontal stress in cylindrical coordinates are shown in Fig. 13. The stress averaging for the complete tensor

$$\sigma_{ij}^{a} = \frac{1}{V_a} \sum_{q=1}^{N_a} V_p \sigma_{ij}^{p} \tag{13}$$

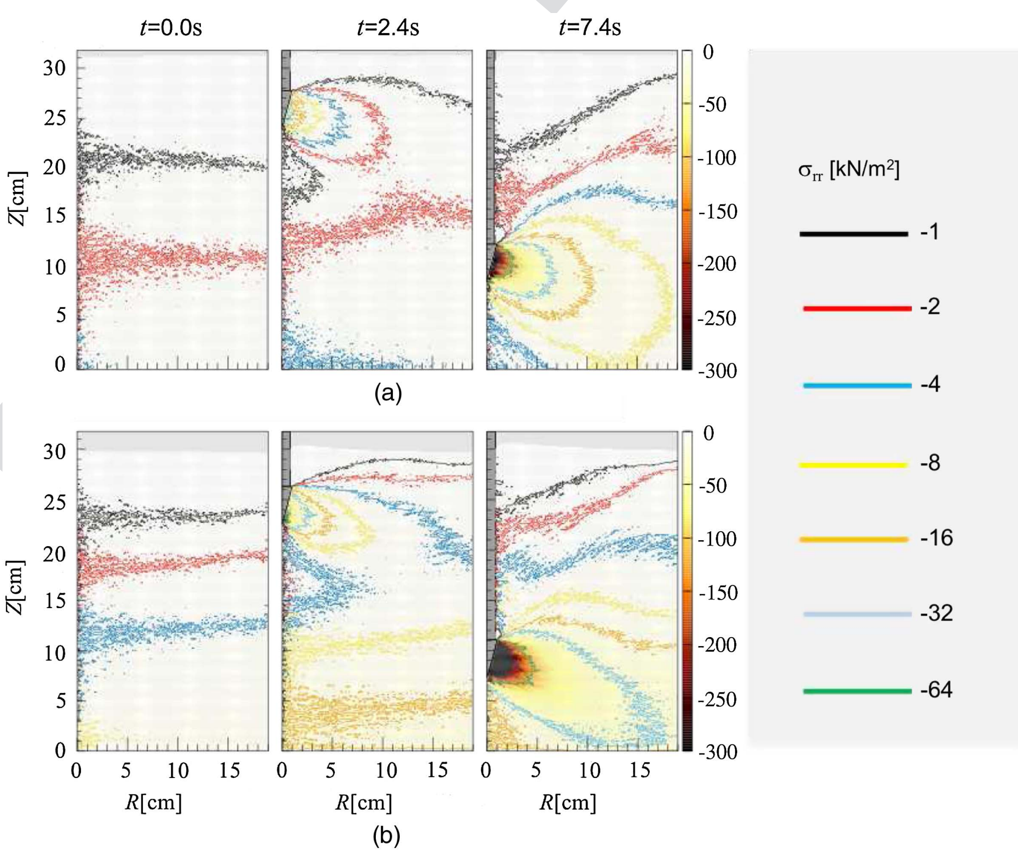

F13:1 **Fig. 13.** Evolution of the horizontal stress component in the (a) settled; and (b) compacted samples.

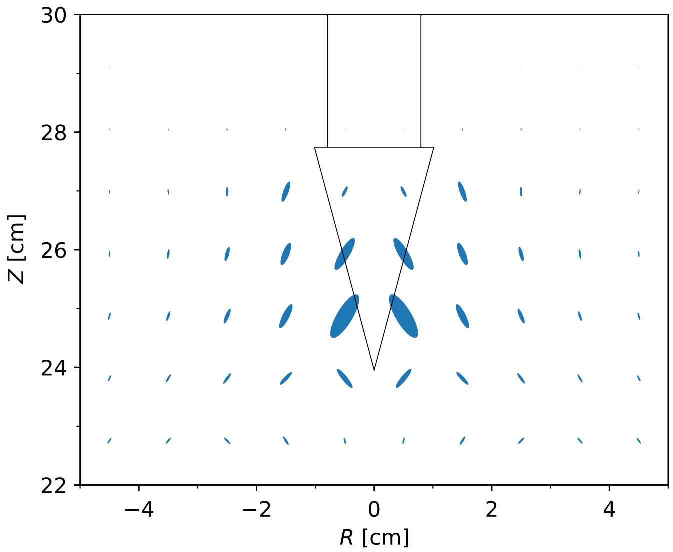

Fig. 14. Stress ellipsoids in the r-z plane indicating both principal stress ratio and principal axes rotation.

is performed over axially centered annulus regions, with V_a being the volume of the ath annulus. The annulus grid dimensions are 152 along the radius and 240 along the height of the cylinder. Grid resolution for averaging of principal stress (Fig. 14) is 19 × 30 grid intervals.

An important aspect of the comparison of settled versus compacted samples seen from Fig. 13 is the relatively higher horizontal stress in the compacted specimen. It is clear from the general cone index trend shown in Fig. 7 that the cone resistance increases with confining stress. Therefore, it is reasonable that some of the higher cone resistance observed for the dense specimen might be caused by the residual stress created by the compaction process. Both the settled and compacted specimens displayed similar distributions of vertical stress, with only a small deviation from a geostatic distribution occurring near the edges of the container. Thus it appears reasonable that the higher horizontal stress in the compacted specimen is caused by the compaction process.

Particle Rotation, Shear Localization, and Failure State

Shear localization can be inferred from displacement profiles, volume changes, and particle rotations. As a point of reference, simulated plane strain tests all displayed concentrations of these three attributes along localization planes at failure. The material grid in the plane strain tests clearly contained dislocations at the site of localization in those tests. The localized band was apparent as increases in both porosity and increased particle rotation. None of the cone simulation results indicated similar evidence of localized deformation zones.

The averaged particle rotation is shown in Fig. 15. Large rotations of particles immediately surrounded the probe, with a concentration at the cone tip. Although some general rotations are suggested by the material grid rotation, the high individual particle rotations within the grid cells indicate intense plastic response. Recall that the rotation of individual particles is not part of the general continuum deformation in which rotation is a result of deformation gradients. Rather, the particle rotations are indicative of *relative* particle rotations that cause contact slip.

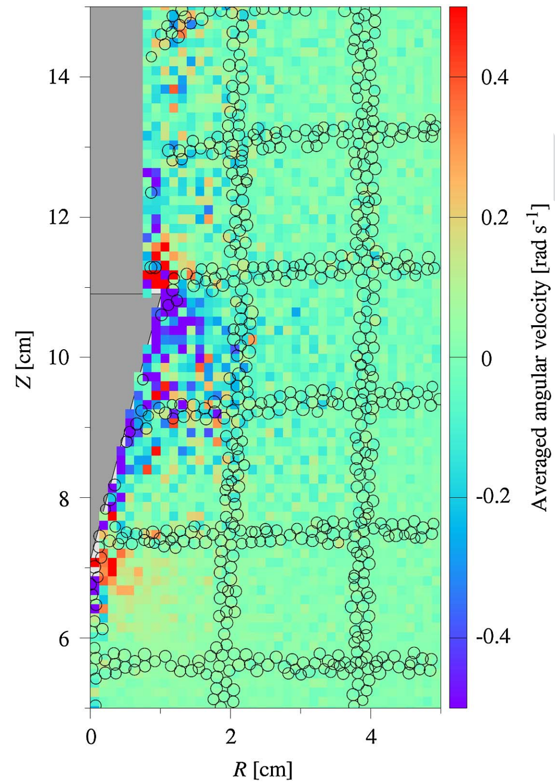

Fig. 15. Averaged particle rotation for a compacted specimen with no overburden.

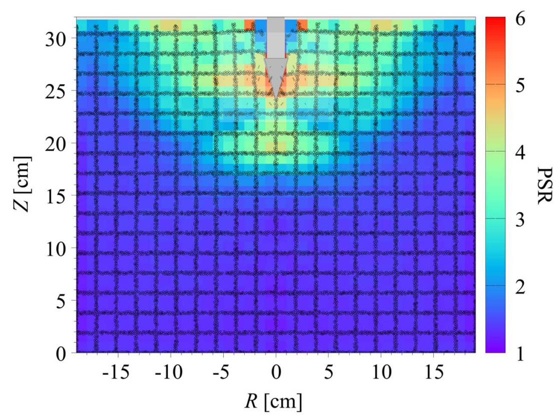

Fig. 16. Principal stress ratio, σ_1/σ_3, in the r-z plane.

The observation of particle rotation in Fig. 15 is supported by the distribution of the principal stress ratio, σ_1/σ_3, shown in Fig. 16. The high stress ratios near the cone show the soil to be in a state of failure. The strong rotation of principal stress shown in Fig. 14 also supports this interpretation. The zone of high stress ratio extends well in front of the advancing cone.

Discussion

The results of the DEM simulated CPT indicated good agreement with experimental cone penetration data (Fig. 7). It is clearly possible to adjust parameters to obtain a wide range of responses provided the porosity is included in the calibration process. The soil porosity is a state established by the particle placement procedure rather than a particle-scale property that can be simply assigned. Moreover, the particle size distribution was chosen for computational convenience to meet resolution requirements and is more like the element size in a finite-element analysis rather than a micromechanical attribute. As a result, neither the particle size nor the porosity can be directly related to micromechanical characteristics, but were chosen here to approximate phenomenological soil behavior.

The initialization method used in this work generally is a significant improvement over methods based on sedimentation; complex boundary geometries are easy to accommodate and very limited displacement is needed to reach the initial state. The methods to reach the initial state, however, are still ad hoc and include some combination of free settlement and compacting by surcharging. For the cone penetration problem, compaction is a simple approach that might not be so attractive for other geotechnical applications with more complex problem domains. The initial stress state induced by compaction or other methods influences behavior, yet is difficult to control. Thus the familiar geotechnical concepts of density and consolidation state are uncertain and difficult to specify. Achieving the initial state is also a problem in nonlinear finite-element analyses even though the relevant quantities can simply be assigned to the elements.

Solid boundary constraints cause alignment of the particles near the constraining boundaries. Layering of particles near the walls is readily observed in Fig. 17 where the condition is illustrated for both the plane strain test apparatus and the cylindrical test cell. Particle layering constitutes a spurious boundary effect that can be limited by reduction in particle size.

At the microscopic scale, the particle kinematics, displacements, and displacement velocities also yield results consistent with those found in the literature (Figs. 7–10). In general, all cases show an increased porosity around the cone, showing an interesting volume change behavior as a response to cavity expansion. Fig. 11 shows that with the application of an overburden pressure, volume expansion is reduced around the cone. It was observed that although the suppression of volumetric expansion by increased stress is expected, there is no clear mechanism in the contact properties to predict such behavior. The general mechanisms contributing to a stress effect on volume change warrant further research.

Shear localization was not directly observed in the CPT simulations. In the case of the cone simulation, localization was not apparent from the displaced grid (Figs. 8 and 11) and the increase in porosity was distributed around the cone rather than along any localized zone. Particle rotations shown in Fig. 15 are distributed around the cone apparently driven by the advancing cone rather than by shear localization. However, a network of particle groups with significant rotations appear to form under the advancing cone tip that signify possible localization zones. Therefore, the cone passes the shear band before significant dislocation can develop. Despite the lack of evidence for distinct shear bands, significant rotation appears to form in the vicinity of the cone, implying the development of a highly plasticized zone as the cone advances.

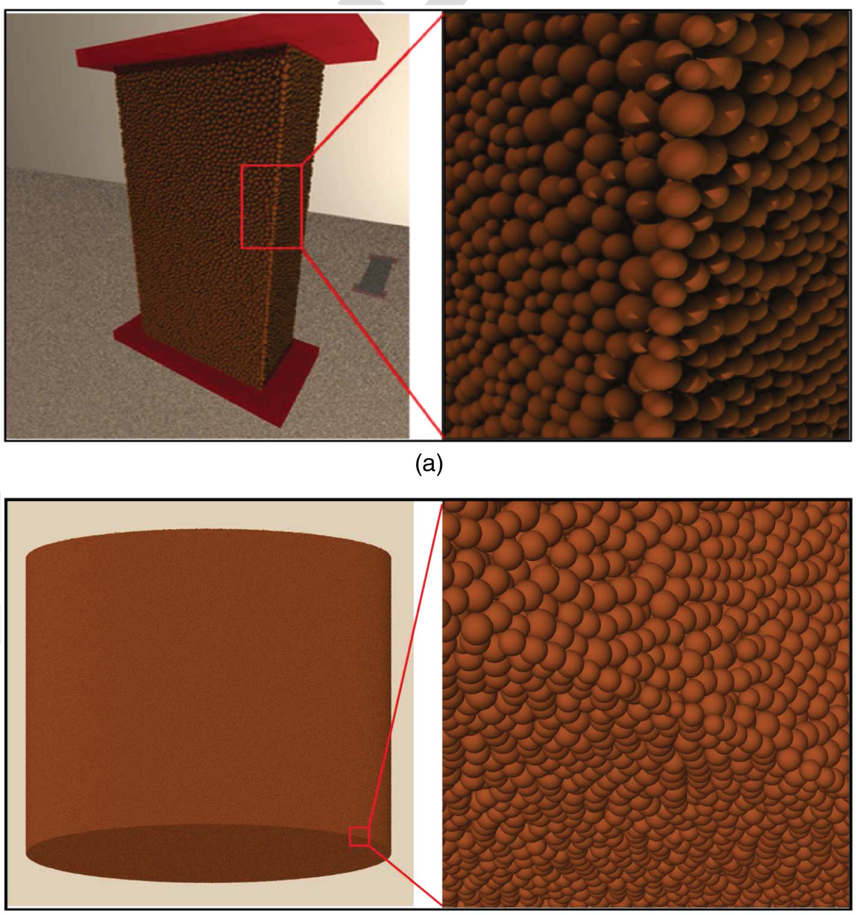

(a)

(b)

F17:1 **Fig. 17.** Particles arrayed along solid boundaries in (a) plane strain test; and (b) testing vessel.

Conclusion

DEM is a potentially valuable tool for analysis of prototype-scale problems with large discontinuous deformations. In the case of the cone penetrometer, realistic simulations were produced including effects of stress field and density.

Prototype-scale analyses differ from those applied to micromechanical studies because the particle-scale details are not necessarily reproduced. Computational resources limit the number of particles that can be simulated, with the result that neither the mean diameter nor the relative particle-scale distribution can be reproduced. The particle shape is generally taken to be spherical as a computational expedient. Particle rolling resistance was applied through an exaggerated contact moment. The interparticle contact properties can not be determined from micromechanical experiments but rather are tied to standard laboratory tests. Calibration consisted of parametric analyses focused on initial stiffness, shape of stress-strain curve, peak strength, and ability to model realistic shear bands.

Several simulations of a specialized cone penetrometer used for mobility assessment illustrate key issues in applying DEM analyses at the prototype scale. Particle kinematics were assessed from marking selected particles as part of a material grid. At the grid scale, particles generally followed affine motion, although at the finer particle scale diffusive motion was possible, especially near the cone tip. In general, particles initially within a material grid cell remained within that cell even after very large expansive displacements. Therefore, the solid volume within each cell remained constant and porosity varied as the total cell volume varied.

The effect of confining pressure was tested by applying a vertical surcharge load at the top of the specimen. The reduced volumetric expansion observed at higher confining stress was in line with expected soil behavior, although nothing in the DEM contact laws explicitly prescribes a confining stress effect. The cause of the predicted confining stress effect requires further investigation.

There is a small boundary effect related to the alignment of particles along the rigid boundaries. Such effects can be reduced by using smaller particles.

Porosity and initial stress had a major effect on the cone resistance, which requires special attention because neither are prescribed contact material properties but are the result of particle placement procedure. In the case of the laboratory calibration chamber tests, the lower porosity specimens were compacted rather than settled, which created larger horizontal residual stresses. These results must be interpreted with the knowledge that higher residual stress might be correlated with higher density, thus making the causality inferred from correlations to higher cone resistance uncertain.

Acknowledgments

This material is based upon research conducted under contract W9I2HZ-17-C-0021 with the US Army Engineer Research and Development Center (ERDC). The views and conclusions contained herein are those of the authors and should not be interpreted as necessarily representing the official policies or endorsements, either expressed or implied, of ERDC or the US Government. Distribution Statement A: Approved for public release: distribution unlimited. Computational resources at the Mississippi State University High Performance Computing Collaboratory (HPC^2) center (Talon, Shadow) and ERDC High Performance Computing Modernization Program (HPCMP) (Garnet and Topaz) were used.

References

Abu-Farsakh, M. Y., G. Z. Voyiadjis, and M. T. Tumay. 1998. "Numerical analysis of the miniature piezocone penetration tests (PCPT) in cohesive soils." *Int. J. Numer. Anal. Methods Geomech.* 22 (10): 791–818. https://doi.org/10.1002/(SICI)1096-9853(1998100)22:10<791::AID-NAG941>3.0.CO;2-6.

Ahmadi, M. M., P. M. Byrne, and R. G. Campanella. 2005. "Cone tip resistance in sand: Modeling, verification, and applications." *Can. Geotech. J.* 42 (4): 977–993. https://doi.org/10.1139/t05-030.

Alshibli, K. A., and S. Sture. 2000. "Shear band formation in plane strain experiments of sand." *J. Geotech. Geoenviron. Eng.* 126 (6): 495–503. https://doi.org/10.1061/(ASCE)1090-0241(2000)126:6(495).

Arroyo, M., J. Butlanska, A. Gens, F. Calvetti, and M. Jamiolkowski. 2011. "Cone penetration tests in a virtual calibration chamber." *Géotechnique* 61 (6): 525–531. https://doi.org/10.1680/geot.9.P.067.

Berger, K. J., and C. M. Hrenya. 2014. "Challenges of DEM. II: Wide particle size distributions." *Powder Technol.* 264 (Sep): 627–633. https://doi.org/10.1016/j.powtec.2014.04.096.

Butlanska, J., M. Arroyo, A. Gens, and C. O'Sullivan. 2013. "Multi-scale analysis of cone penetration test (CPT) in a virtual calibration chamber." *Can. Geotech. J.* 51 (1): 51–66. https://doi.org/10.1139/cgj-2012-0476.

Carrillo, A. R., D. A. Horner, J. F. Peters, and J. E. West. 1996. "Design of a large scale discrete element soil model for high performance computing systems." In *Proc., 1996 ACM/IEEE Conf. on Supercomputing*, 1–15. New York: IEEE.

Cleary, P. W. 2009. "Industrial particle flow modelling using discrete element method." *Eng. Computations* 26 (6): 698–743. https://doi.org/10.1108/02644400910975487.

Cleary, P. W., and M. Frank. 2006. *Three-dimensional discrete element simulation of axisymmetric collapses of granular columns*. Technical Rep. No. 44710. Kaiserslautern, Germany: Technische Universitat Kaiserslautern.

Cleary, P. W., N. Stokes, and J. Hurley. 1997. "Efficient collision detection for three dimensional super-ellipsoidal particles." In *Proc., 8th Int. Computational Techniques and Applications Conf.: CTAC'97*. Canberra, Australia: Australian and New Zealand Industrial and Applied Mathematics Division of the Australian Mathematical Society.

Coetzee, C. 2017. "Review: Calibration of the discrete element method." *Powder Technol.* 310 (Apr): 104–142. https://doi.org/10.1016/j.powtec.2017.01.015.

Cole, D. M., and J. F. Peters. 2007. "A physically based approach to granular media mechanics: Grain-scale experiments, initial results and implications to numerical modeling." *Granular Matter* 9 (5): 309–321. https://doi.org/10.1007/s10035-007-0046-2.

Cundall, P. A. 2001. "A discontinuous future for numerical modelling in geomechanics?" *Proc. Inst. Civ. Eng. Geotech. Eng.* 149 (1): 41–47. https://doi.org/10.1680/geng.2001.149.1.41.

Cundall, P. A., and O. D. L. Strack. 1979. "A discrete numerical model for granular assemblies." *Géotechnique* 29 (1): 47–65. https://doi.org/10.1680/geot.1979.29.1.47.

Falagush, O., G. R. McDowell, and H.-S. Yu. 2015. "Discrete element modeling of cone penetration tests incorporating particle shape and crushing." *Int. J. Geomech.* 15 (6): 04015003. https://doi.org/10.1061/(ASCE)GM.1943-5622.0000463.

Fan, S., B. Bienen, and M. Randolph. 2018. "Stability and efficiency studies in the numerical simulation of cone penetration in sand." *Géotechnique Lett.* 8 (1): 13–18. https://doi.org/10.1680/jgele.17.00105.

Feng, Y., K. Han, D. Owen, and J. Loughran. 2009. "On upscaling of discrete element models: Similarity principles." *Eng. Computations* 26 (6): 599–609. https://doi.org/10.1108/02644400910975405.

Ferellec, J.-F., and G. R. McDowell. 2010. "A method to model realistic particle shape and inertia in DEM." *Granular Matter* 12 (5): 459–467. https://doi.org/10.1007/s10035-010-0205-8.

Furuichi, M., D. Nishiura, O. Kuwano, A. Bauville, T. Hori, and H. Sakaguchi. 2018. "Arcuate stress state in accretionary prisms from real-scale numerical sandbox experiments." *Sci. Rep.* 8 (1): 8685. https://doi.org/10.1038/s41598-018-26534-x.

Goodman, C. C., F. Vahedifard, and J. F. Peters. 2017. "Kinematics of shear banding in 3D plane strain DEM."In *Proc., Geotechnical Frontiers 2017*, 519–528. Reston, VA: ASCE.

Gui, M., and D.-S. Jeng. 2009. "Application of cavity expansion theory in predicting centrifuge cone penetration resistance." *Open Civ. Eng. J.* 3: 1–6. https://doi.org/10.2174/1874149500903010001.

Holmen, J. K., L. Olovsson, and T. Børvik. 2017. "Discrete modeling of low-velocity penetration in sand." *Comput. Geotech.* 86 (Jun): 21–32. https://doi.org/10.1016/j.compgeo.2016.12.021.

Hopkins, M. 2014. "Polyhedra faster than spheres?" *Eng. Comput.* 31 (3): 567–583. https://doi.org/10.1108/EC-09-2012-0211.

Horner, D. A., A. R. Carrillo, J. F. Peters, and J. E. West. 1998. "High resolution soil vehicle interaction modeling." *Mech. Struct. Mach.* 26 (3): 305–318. https://doi.org/10.1080/08905459708945497.

Huang, W., D. Sheng, S. Sloan, and H. Yu. 2004. "Finite element analysis of cone penetration in cohesionless soil." *Comput. Geotech.* 31 (7): 517–528. https://doi.org/10.1016/j.compgeo.2004.09.001.

Jarast, P., and M. Ghayoomi. 2018. "Numerical modeling of cone penetration test in unsaturated sand inside a calibration chamber." *Int. J. Geomech.* 18 (2): 04017148. https://doi.org/10.1061/(ASCE)GM.1943-5622.0001052.

Jiang, M., H. H. Zhu, and D. Harris. 2008. "Classical and non-classical kinematic fields of two-dimensional penetration tests on granular ground by discrete element method analyses." *Granular Matter* 10 (6): 439. https://doi.org/10.1007/s10035-008-0107-1.

Jin, Y.-F., Z.-Y. Yin, Z.-X. Wu, and A. Daouadji. 2018. "Numerical modeling of pile penetration in silica sands considering the effect of grain breakage." *Finite Elem. Anal. Des.* 144 (May): 15–29. https://doi.org/10.1016/j.finel.2018.02.003.

Johnson, D. H., F. Vahedifard, B. Jelinek, and J. F. Peters. 2017. "Micromechanical modeling of discontinuous shear thickening in granular media-fluid suspension." *J. Rheol.* 61 (2): 265–277. https://doi.org/10.1122/1.4975027.

Kawaguchi, T., T. Tanaka, and Y. Tsuji. 1998. "Numerical simulation of two-dimensional fluidized beds using the discrete element method (comparison between the two-and three-dimensional models)." *Powder Technol.* 96 (2): 129–138. https://doi.org/10.1016/S0032-5910(97)03366-4.

Kiousis, P. D., G. Z. Voyiadjis, and M. T. Tumay. 1988. "A large strain theory and its application in the analysis of the cone penetration mechanism." *Int. J. Numer. Anal. Methods Geomech.* 12 (1): 45–60. https://doi.org/10.1002/nag.1610120104.

Knuth, M. A., J. B. Johnson, M. A. Hopkins, R. J. Sullivan, and J. Moore. 2012. "Discrete element modeling of a mars exploration rover wheel in granular material." *J. Terramech.* 49 (1): 27–36. https://doi.org/10.1016/j.jterra.2011.09.003.

Kotrocz, K., A. M. Mouazen, and G. Kerényi. 2016. "Numerical simulation of soil–cone penetrometer interaction using discrete element method." *Comput. Electron. Agric.* 125 (Jul): 63–73. https://doi.org/10.1016/j.compag.2016.04.023.

Kuhn, M. R. 2003. "Smooth convex three-dimensional particle for the discrete-element method." *J. Eng. Mech.* 129 (5): 539–547. https://doi.org/10.1061/(ASCE)0733-9399(2003)129:5(539).

Lu, M., and G. R. McDowell. 2007. "The importance of modelling ballast particle shape in the discrete element method." *Granular Matter* 9 (1–2): 69. https://doi.org/10.1007/s10035-006-0021-3.

Markauskas, D., R. Kačianauskas, A. Džiugys, and R. Navakas. 2010. "Investigation of adequacy of multi-sphere approximation of elliptical particles for DEM simulations." *Granular Matter* 12 (1): 107–123. https://doi.org/10.1007/s10035-009-0158-y.

Markauskas, D., R. Kačianauskas, and M. Šukšta. 2002. "Modeling the cone penetration test by the finite element method." *In Foundations of civil and environmental engineering*. Poznań, Poland: Publishing House of Poznań University of Technology.

Mayne, P. 2006. "In-situ test calibrations for evaluating soil parameters." In Vol. 3 of *Proc., Int. Workshop on Characterisation and Engineering Properties of Natural Soils (Natural Soils 2006)*, edited by T. Tan, K. Phoon, D. Hight, and S. Leroueil, 1601–1652. London: Taylor & Francis.

Melzer, K.-J. 1971. *Measuring soil properties in vehicle mobility research. Report 4. Relative density and cone penetration resistance*. Rep. No. 3-652. Vicksburg, MS: US Army Engineer Waterways Experiment Station.

Mühlhaus, H., and I. Vardoulakis. 1987. "The thickness of shear bands in granular materials." *Géotechnique* 37 (3): 271–283. https://doi.org/10.1680/geot.1987.37.3.271.

Nezami, E. G., Y. M. Hashash, D. Zhao, and J. Ghaboussi. 2004. "A fast contact detection algorithm for 3-D discrete element method." *Comput. Geotech.* 31 (7): 575–587. https://doi.org/10.1016/j.compgeo.2004.08.002.

O'Sullivan, C. 2011. "Particle-based discrete element modeling: Geomechanics perspective." *Int. J. Geomech.* 11 (6): 449–464. https://doi.org/10.1061/(ASCE)GM.1943-5622.0000024.

Peters, J. F., M. A. Hopkins, R. Kala, and R. E. Wahl. 2009. "A poly-ellipsoid particle for non-spherical discrete element method." *Eng. Comput.* 26 (6): 645–657. https://doi.org/10.1108/02644400910975441.

Peters, J. F., M. Muthuswamy, J. Wibowo, and A. Tordesillas. 2005. "Characterization of force chains in granular material." *Physical Rev. E* 72 (4): 041307. https://doi.org/10.1103/PhysRevE.72.041307.

Priddy, J. D., E. S. Berney, and J. F. Peters. 2012. "Effect of near-surface hydrology on soil strength and mobility." *Geol. Soc. London, Spec. Publ.* 362 (1): 301–320. https://doi.org/10.1144/SP362.17.

Salgado, R., J. K. Mitchell, and M. Jamiolkowski. 1997. "Cavity expansion and penetration resistance in sand." *J. Geotech. Geoenviron. Eng.* 123 (4): 344–354. https://doi.org/10.1061/(ASCE)1090-0241(1997)123:4(344).

Salot, C., P. Gotteland, and P. Villard. 2009. "Influence of relative density on granular materials behavior: DEM simulations of triaxial tests." *Granular Matter* 11 (4): 221–236. https://doi.org/10.1007/s10035-009-0138-2.

Stevens, M. T., B. W. Towne, G. L. Mason, J. D. Priddy, J. E. Osorio, and C. A. Barela. 2013. *Procedures for one-pass vehicle cone index* (VCI_1) *determination for acquisition support*. Rep. No. ERDC/GSL SR-13-2. Vicksburg, MS: US Army Corps of Engineers Research and Development Center.

Ting, J. M., B. T. Corkum, C. R. Kauffman, and C. Greco. 1989. "Discrete numerical model for soil mechanics." *J. Geotech. Eng.* 115 (3): 379–398. https://doi.org/10.1061/(ASCE)0733-9410(1989)115:3(379).

Tordesillas, A., S. Pucilowski, D. M. Walker, J. Peters, and M. Hopkins. 2012. "A complex network analysis of granular fabric evolution in three-dimensions." *Dynam. Cont. Dis. Ser. B* 19 (Jan): 471–495.

Tordesillas, A., J. Zhang, and R. Behringer. 2009. "Buckling force chains in dense granular assemblies: Physical and numerical experiments." *Geomech. Geoeng.: Int. J.* 4 (1): 3–16. https://doi.org/10.1080/17486020902767347.

van den Berg, P., R. de Borst, and H. Huétink. 1996. "An Eulerean finite element model for penetration in layered soil." *Int. J. Numer. Anal. Methods Geomech.* 20 (12): 865–886. https://doi.org/10.1002/(SICI)1096-9853(199612)20:12<865::AID-NAG854>3.0.CO;2-A.

Vardoulakis, I. 1980. "Shear band inclination and shear modulus of sand in biaxial tests." *Int. J. Numer. Anal. Methods Geomech.* 4 (2): 103–119. https://doi.org/10.1002/nag.1610040202.

Walton, O. R., and R. L. Braun. 1986. "Stress calculations for assemblies of inelastic speres in uniform shear." *Acta Mech.* 63 (1–4): 73–86. https://doi.org/10.1007/BF01182541.

Yu, H. 2006. "The first James K. Mitchell lecture in situ soil testing: From mechanics to interpretation." *Geomech. Geoeng.: Int. J.* 1 (3): 165–195. https://doi.org/10.1080/17486020600986884.

Yu, H., and G. Houlsby. 1991. "Finite cavity expansion in dilatant soils: Loading analysis." *Géotechnique* 41 (2): 173–183. https://doi.org/10.1680/geot.1991.41.2.173.

Zhang, Z., and Y.-H. Wang. 2015. "Three-dimensional dem simulations of monotonic jacking in sand." *Granular Matter* 17 (3): 359–376. https://doi.org/10.1007/s10035-015-0562-4.

Queries

1. Please check and confirm whether all the corrections are carried out correctly.